GSA Data Repository 2017253

Diaz, M.R., Eberli, G.P., Blackwelder, P., Phillips, B., and Swart, P.K., 2017, Microbially mediated organomineralization in the formation of ooids: Geology, doi:10.1130/G39159.1.

Supplemental Material

METHODS

Sample collection and handling. Sediments consisting of an admixture of surface and subsurface sediments (upper 2.5 cm) were collected and preserved in the field. For petrographic thin sections the field samples were washed with distilled water and embedded in epoxy. The SEM samples were preserved *in situ* with 70% ethanol or 4.5% formaldehyde and kept at 5°C until further analysis, whereas samples for ACC determination ($^{13}C\{^{1}H\}$ CPMAS–NMR analysis) were preserved following the protocol of Foran et al. (2013) and kept in 100% ethanol at 5°C until further analysis.

SEM Analysis. Field samples preserved in formaldehyde and ethanol were further processed in the laboratory with 2% gluteraldehyde and 0.2 μm millepore filtered 0.05M sodium cacodylate buffered seawater to preserve and stabilize the structures of the microbial cells and keep their integrity as close as possible to their living state. The samples were rinsed three times in the seawater buffer, dehydrated in a graded series of ethanol (20, 50, 70, 95 and 100%), and dried in three changes of Hexamethyldisiloxane (HMDS). For conductivity, the samples were coated with Pd in a plasma sputter coater. Imaging was conducted in a field emission SEM (Philips XL-30).

EPS Detection.

EPS identification was based on morphological attributes and conventional SEM descriptions of the EPS matrix, which can range from slimy thin filaments, mucous,

smooth film structures, translucent dehydrated films, honey comb structures, etc (Jones and Peng, 2012; 2014; Peng and Jones; 2013; Handley et al, 2008; Flemming and Wingender, 2010).

Microbial Identification. Diatoms were identified by the phenotipic characteristics of their silicified cell walls (frustules) while bacteria and fungi follow conventional morphological traits such as cell shape, size, and surface structure of cells, etc (Hawksworth 1988; Hasle and Syvertsen 1996; Bergmans et al, 2005).

Solid State NMR Spectroscopy. The $^{13}C\{^{1}H\}$ cross-polarization magic-angle-spinning (CPMAS) NMR analyses were conducted on a 400 MHz (9.4 T) Varian Infinity Plus spectrometer (Varian Associates Inc, Palo Alto, USA) operating at 100.6 MHz for ^{13}C and 399.76 MHz for ^{1}H. Duplicate samples were contained in a Varian/Chemagnetics 'T3' type probe assembly configured for 7.5 mm rotors (outer diameter) and spun at 4 kHz. The instrument running conditions used a standard ramped-CP pulse sequence consisting of an 8 μs 90° ^{1}H excitation pulse, a 1.5 ms $^{1}H \rightarrow {}^{13}C$ contact period during which the ^{13}C excitation was ramped ±4 kHz about the first sideband match condition, and a 1 s relaxation delay. A 50 kHz ^{1}H decoupling field with two pulse phase modulation (TPPM) was applied during acquisition. The final spectra represent 150,000-200,000 acquisitions. The ^{13}C and ^{1}H chemical shifts are referenced relative to tetramethylsilane (TMS) using adamantane as a secondary internal standard ($\boldsymbol{\delta}^{13}C$ = 38.6 and $\boldsymbol{\delta}^{2}H$ = 2.0 ppm). Synthetic ACC and synthetic aragonite were used as external reference standards both of which have $\boldsymbol{\delta}^{13}C$ of 169 and 171 ppm, respectively. Both compounds were synthetized according to established methods (Michel et al., 2008). The line fitting analysis of the CPMAS fit was used to eliminate experimental noise while deconvolution of the

carbonate region – performed with the instrument software Varian Spinsight – employed the least square fit to a sum of Gaussian-shaped curves to differentiate the crystalline and non-crystalline contributions of the spectrum and to further improve the resolution of individual spectral components (Mehring, 1983; Morris et al. 1997). Line shape distortions of the spectrum were removed using TMS as a reference signal prior to deconvolution analysis (Rabenstein and Keire 1990; Morris et al. 1997.)

FIGURE LEGENDS

Fig DR1. Map of the Bahamas depicting the sampling localities.

Fig DR2. Photomicrographs of Bahamian ooids. **A-B**) Ooids from Joulters Cay (mean = 460 μm). Note the well-preserved exterior and defined peloidal nuclei. Some of the ooids show fingerprints of microboring activity and accumulation of organic material (dark color) entrapped within the cortical laminations. **C-D**) Ooids from Cat Cay (mean = 361 μm). Cat Cay ooids show well developed cortical laminations and peloidal nuclei. Note that some ooids show heavy micritization along the periphery of the nucleus. **E-F**) Ooids from Shroud Cay (mean = 464 μm) are also well preserved with well lamination pattern, some of which show micritization. Some ooids display enlarged peloidal nuclei, while others bear foraminiferous or shell fragments (arrow). **G-H)** Ooids from Butterfly Beach (mean = 180 μm) are characterized by being the smallest in size with thin coatings around the nucleus. These ooids show few endolithic borings or areas indicative of micritization. **I-J)** Well-sorted medium grained ooid sands from Schooner Cays (mean = 450 μm).

Fig DR3. SEM images depicting mineral morphologies in ooids from the Bahamas. **A)** Aragonite baton. **B)** Aragonite needles. **C)** Capped aragonite batons. **D)** Nanograins. **E)** Calcite rhombic crystal. **F)** Plywood-like crystals. **G)** Aragonite crystal bundle with nanograins around them. **H)** Incomplete calcite growth. **I)** Daisy like crystal forms with radial orientation.

Fig DR4. SEM photomicrographs documenting the occurrence of EPS, nanograins and microbes in ooids from the Bahamas. **A)** Scattered distribution of EPS in the outer cortex of an ooid. **B)** A cluster of nanograins in a mucus shield matrix. **C)** EPS inside a pit of an ooid. Note the few scattered nanograins protruding from the polymer matrix. **D)** EPS and nanograins in a shallow depression. **E)** A coccus bacterium embedded in EPS biofilm. **F)** A diatom in proximity to EPS biofilm. **G)** Cocci bacteria entrenched in EPS. **H)** EPS and *Spirulina* sp., an *Oscillatoriales* cyanobacterium. **I)** Filamentous cyanobacteria and fungi colonizing the interior of a cracked ooid. EPS denotes: Extracellular polymeric substance; N: nanograins; D: diatom; b: bacteria; fcy/ff: filamentous cyanobacteria/fungi.

Fig DR5. SEM photomicrographs documenting the ubiquitous presence of diatoms in ooid grains from the active shoals of the Bahamas. **A)** A pennate diatom on a shallow depression in an ooid from Cat Cay. **B)** A pennate diatom in an ooid outer cortex in Joulters Cay. **C)** A cigar shape diatom and associated EPS exudates colonizing the outer surface of an ooid from Butterfly Beach. **D)**. A diatom and a microplate disk of the coccolithophore, *Emiliania huxleyi.* D denotes: diatom; C: coccolithophore.

Fig. DR6. SEM photomicrographs documenting unicellular asexual reproduction and a sulfur globule deposit. **A)** A representation of the splitting of a parental cell into two

daughter cells through binary fission, also observed by Jones et al., (2007, their Fig 6B) in sublacustrine spring deposits. **B)** Bulbous expansion by budding cell division, a mode of reproduction among bacterial lineages within *Cyanobacteria*, *Planctomycetes*, *Firmicutes*, α-*Proteobacteria* (Angert, 2005) and some eukaryotes (Javaux and Knoll 2016, theirs Fig 6.10). **C)** A sulfur globule deposit (yellow arrow) with similar morphology as illustrated by Glunk et al. (2011, their Fig 8c).

REFERENCES CITED

Angert, E.R., 2005, Alternative to binary fission by bacteria: Nature Reviews Microbiology, v. 3, p. 214-224.

Bergmans, L., Moisiadis, P., Van Meerbeek, B., Quirynen, M., and Lambrecht, P., 2005, Microscopic observation of bacteria: review highlighting the use of environmental SEM: International Endodontic Journal, v. 38, p. 775-788.

Flemming, H.C., and Wingender, J., 2010, The biofilm matrix: Nature Reviews Microbiology, v. 8, p. 623-633.

Foran, E., Weiner S., and Fine, M., 2013, Biogenic fish-gut calcium carbonate is a stable amorphous phase in the gilt-head seabream, *Sparus aurata*: Scientific Reports, v. 3, p. 1701 -1705.

Glunk, C, Dupraz, C, Braissant, O., and Visscher, P.T., 2011, Microbially mediated carbonate precipitation in a hypersaline lake, Big Pond Eleutera, Bahamas: Sedimentology, v.58, p. 720-738.

Handley, K.M., Turner, S.J., Campbel, K.A., and Mountain, B.W., 2008, Silicifying biofilm exopolymers on a hotspring microstromatolite: templating nanometer thick laminae, Astrobiology, v. 8, p.747-770.

Hasle, G.R, and Syvertsen, E.E., 1996, Marine Diatoms, *in*: Tomas, C.R., ed., Identifying marine diatoms and dinoflagellates: London, Academic Press, p. 5-385.

Hawksworth, D.L., 1988, Identification. *in:* Hawksworth, D.L., eds, Filamentous fungi: New York, Cambridge University Press, p. 100-114.

Javaux, E.J., and Knoll, A.H., 2016, Micropaleontology of the lower Mesoproterozoic Roper Group, Australia, and implications for early eukaryotic evolution: Journal of Paleontology, http://dx.doi.org/10.1017/jpa.2016.124

Jones, B., de Ronde, C.E.J.,Renaut, R.W., and Owen, R., 2007, Siliceous sublacustrine spring deposits around hydrothermal vents in Lake Taupo, New Zealand: Journal of the Geological Society, v. 164, p. 227-242.

Jones, B., and Peng, X., 2012, Amorphous calcium carbonate associated with biofilms in hot spring deposits: Sedimentary Geology, v. 269/270, p. 58-68.

Jones, B., and Peng, X**.** 2014, Signatures of biologically influenced $CaCO_3$ and Mg-Fe silicate precipitation in hot springs: Case study from Ruidian geothermal area, western Yunnan Province, China: Sedimentology, 61, p. 56-89.

Mehring, H., 1983, Principles of high resolution NMR in solids: NMR-Basic Principles and Progress: Berlin Heidelberg, Springer-Verlag, 344 p.

Michel, F.M., MacDonald, J., Feng, J., Phillips, B.L., Ehm, L., Tarabrella, C., Parise, J.B., and Reeder R. J., 2008, Structural characteristics of synthetic amorphous calcium carbonate: Chemistry of Materials, v. 20, p. 4720 **-** 4728.

Morris, G.A., Barjat, H., and Home, T.J., 1997, Reference deconvolution methods: Progress in Nuclear Magnetic Resonance Spectroscopy, v. 31, p. 197–257.

Peng, X, and Jones, B., 2013, Patterns of biomediated $CaCO_3$ crystal bushes in hot

spring deposits: Sedimentary Geology, v. 294, p. 105-117.

Rabenstein, D.L., and Keire D.A., 1990, Quantitative chemical analysis by NMR: *in* Popov A.I. eds, Modern NMR Techniques and their application in chemistry: New York, Marcel Dekker Inc., p. 323-370.

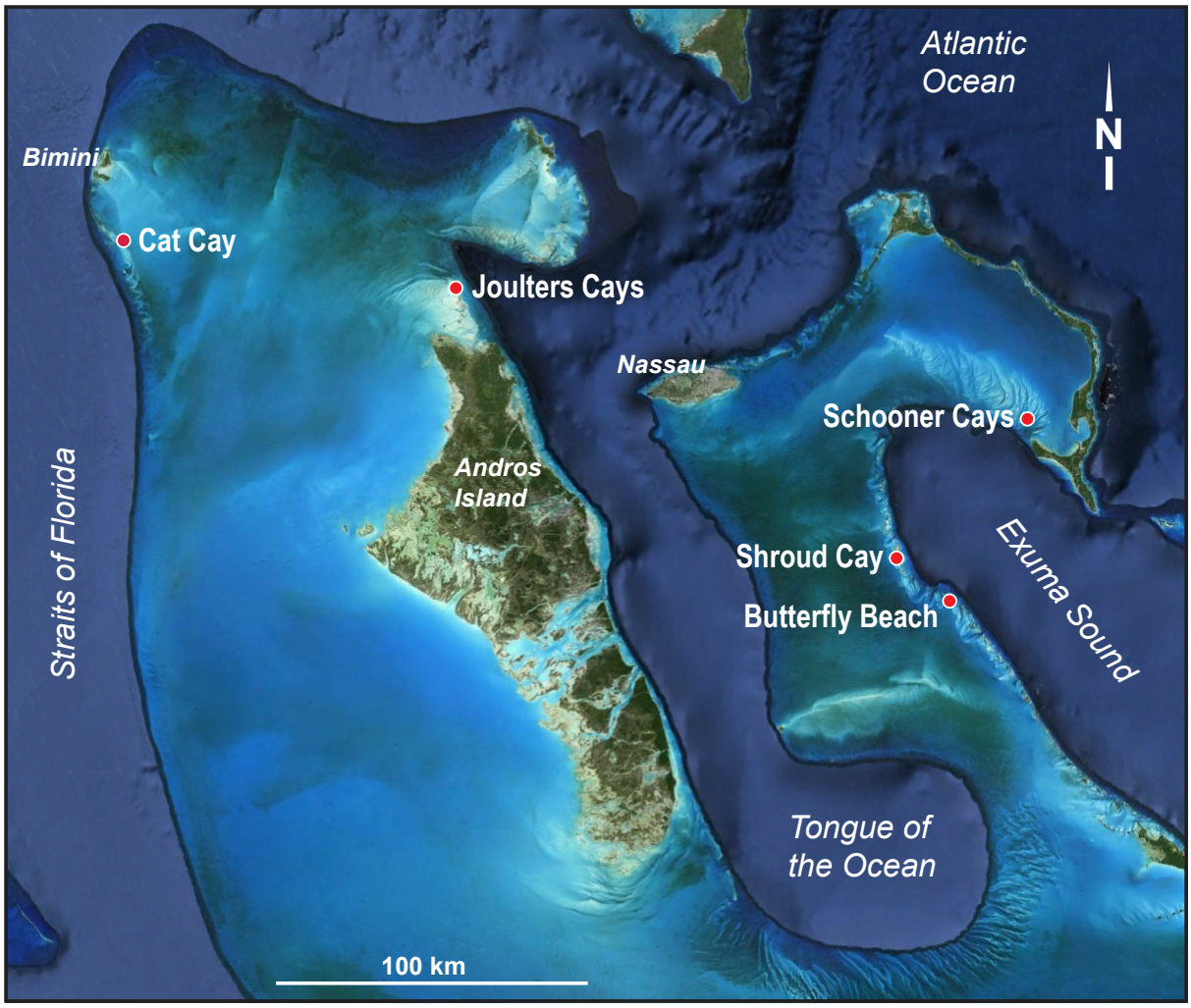
Atlantic Ocean
N
Bimini
Cat Cay
Joulters Cays
Nassau
Schooner Cays
Andros Island
Straits of Florida
Shroud Cay
Butterfly Beach
Exuma Sound
Tongue of the Ocean
100 km

Figure DR1

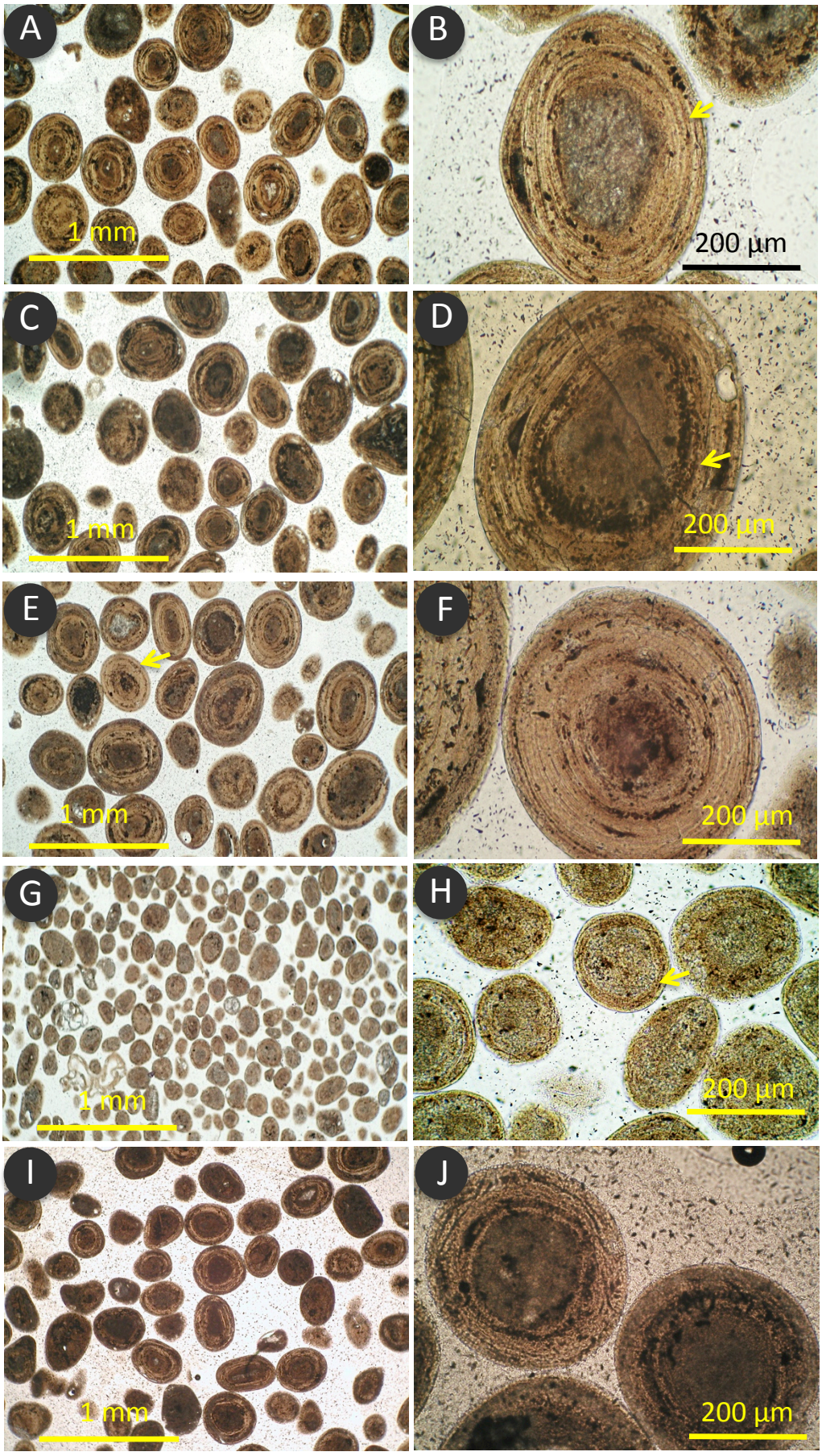
A
1 mm
B
200 µm
C
1 mm
D
200 µm
E
1 mm
F
200 µm
G
1 mm
H
200 µm
I
1 mm
J
200 µm

Figure DR2

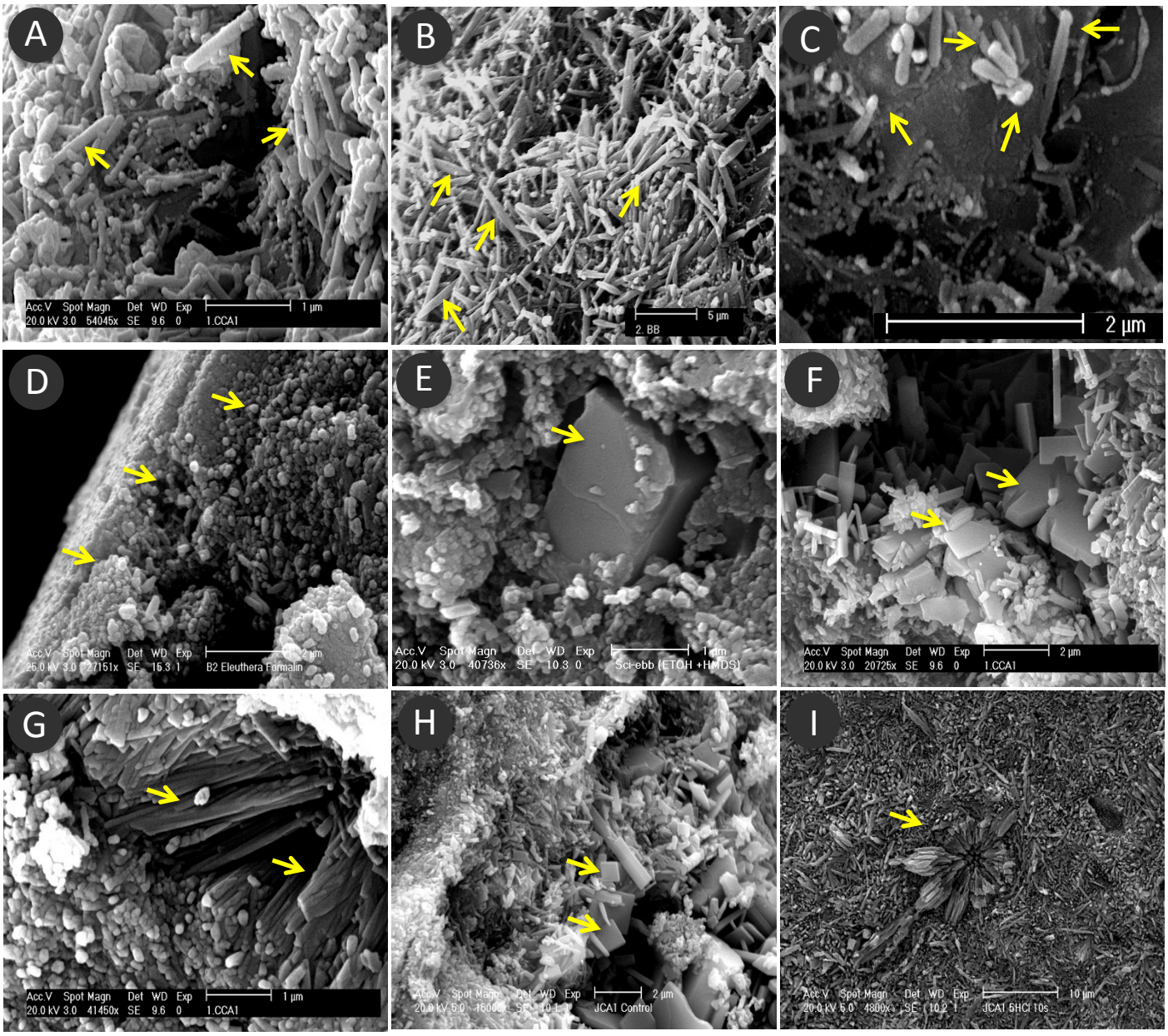
A
Acc.V Spot Magn Det WD Exp
20.0 kV 3.0 54045x SE 9.6 0 1.CCA1
1 µm
B
5 µm
2. BB
C
2 µm
D
Acc.V Spot Magn Det WD Exp
25.0 kV 3.0 27151x SE 16.3 1 B2 Eleuthera Formalin
2 µm
E
Acc.V Spot Magn Det WD Exp
20.0 kV 3.0 40736x SE 10.3 0 Sci-ebb (ETOH +HMDS)
1 µm
F
Acc.V Spot Magn Det WD Exp
20.0 kV 3.0 20725x SE 9.6 0 1.CCA1
2 µm
G
Acc.V Spot Magn Det WD Exp
20.0 kV 3.0 41450x SE 9.6 0 1.CCA1
1 µm
H
2 µm
JCA1 Control
I
10 µm
JCA1 6HCl 10s

Figure DR3

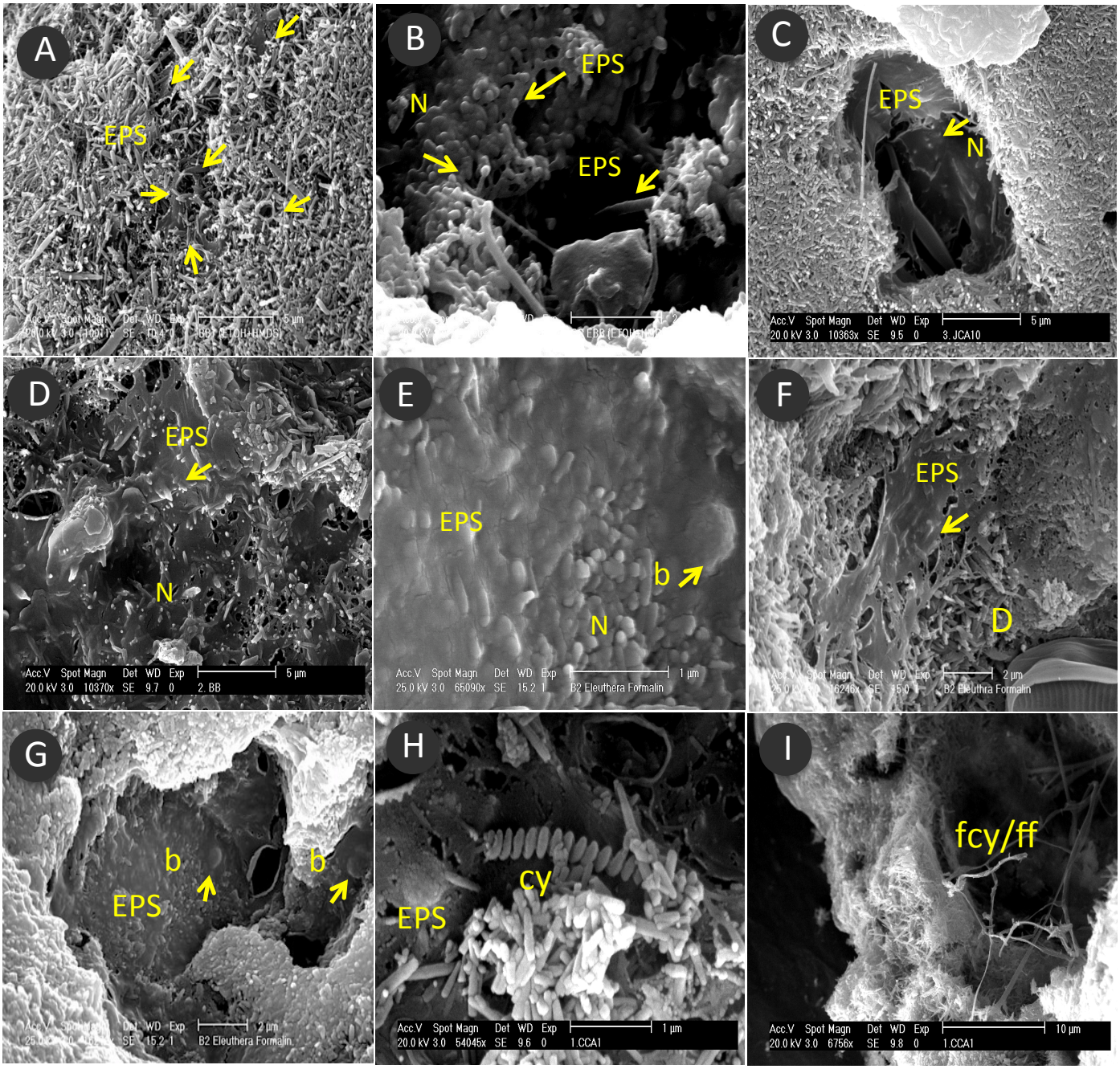
A
EPS
B
EPS
N
EPS
C
EPS
N
D
EPS
N
E
EPS
b
N
F
EPS
D
G
b
b
EPS
H
cy
EPS
I
fcy/ff

Figure DR4

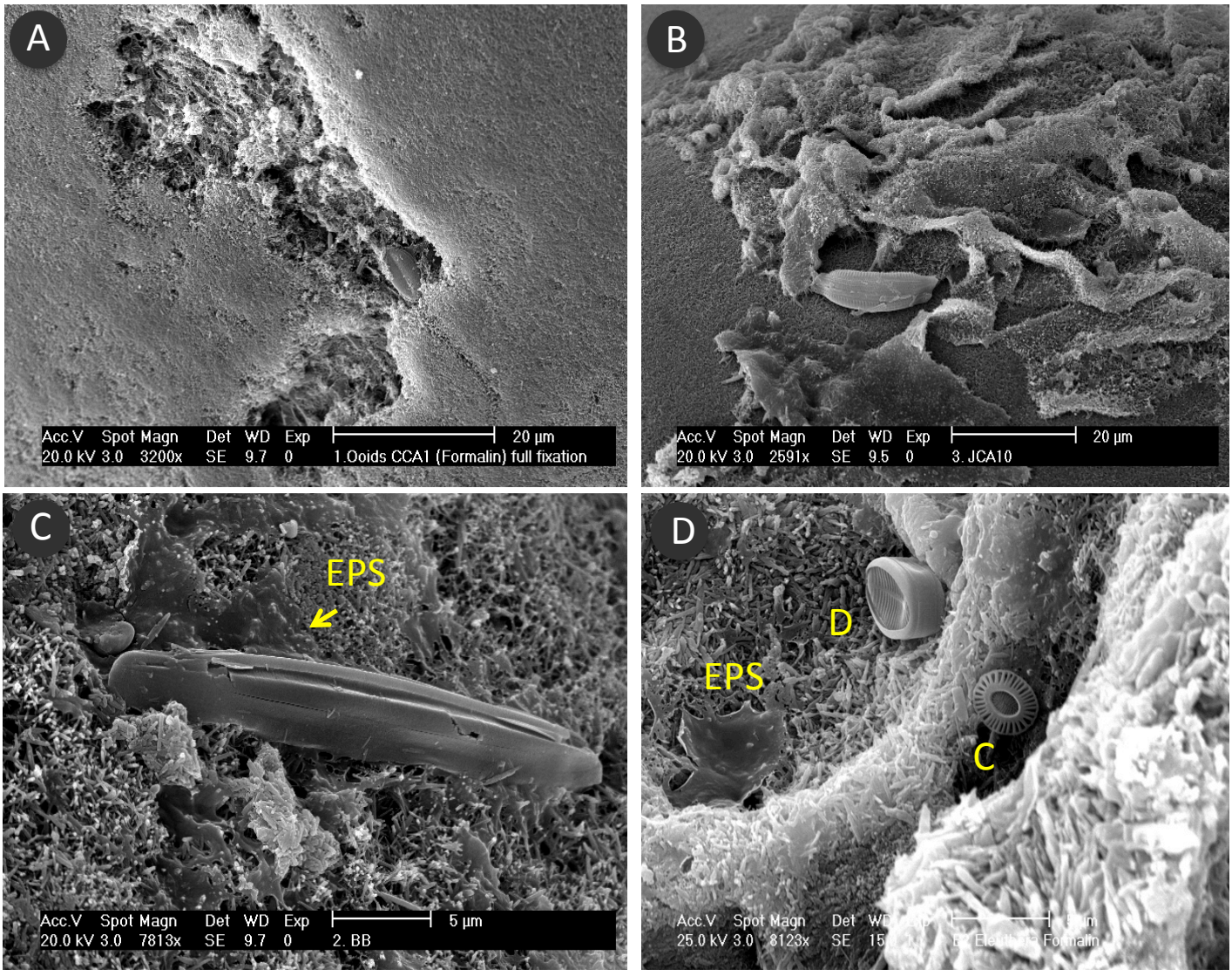
A
Acc.V Spot Magn Det WD Exp 20 µm
20.0 kV 3.0 3200x SE 9.7 0 1.Ooids CCA1 (Formalin) full fixation
B
Acc.V Spot Magn Det WD Exp 20 µm
20.0 kV 3.0 2591x SE 9.5 0 3. JCA10
C
EPS
Acc.V Spot Magn Det WD Exp 5 µm
20.0 kV 3.0 7813x SE 9.7 0 2. BB
D
D
EPS
C
Acc.V Spot Magn Det WD
25.0 kV 3.0 8123x SE 15

Figure DR5

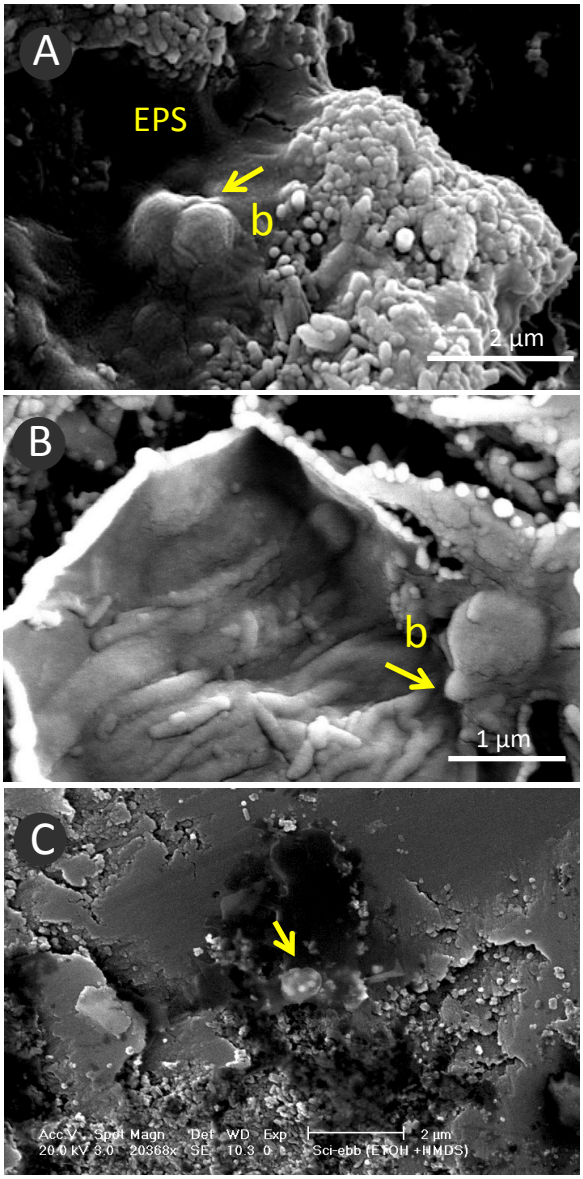
A
EPS
b
2 µm
B
b
1 µm
C
Acc.V Spot Magn Det WD Exp
20.0 kV 3.0 20368x SE 10.3 0
2 µm
Sci-ebb (EtOH +HMDS)

Figure DR6